ChemPubSoc Europe

DOI: 10.1002/celc.201500440

CHEMELECTROCHEM Articles

Oxygen Reduction at Carbon-Supported Lanthanides: The Role of the B-Site

Verónica Celorrio,[a] Ellie Dann,[a] Laura Calvillo,[b] David J. Morgan,[c] Simon R. Hall,[a] and David J. Fermin*[a]

The kinetics of the oxygen reduction reaction (ORR) at carbon-supported transition-metal oxides in alkaline solutions is systematically investigated as a function of the nature of the B-site. The study is focused on $LaBO_3$ (B = Cr, Co, Fe, Mn and Ni) nanoparticles synthesized by using an ionic-liquid route, offering fine control over phase purity and composition. Activity towards the ORR was compared with the commercial Pt/Etek catalyst. Detailed electrochemical analysis employing a rotating ring-disk electrode provides conclusive evidence that the carbon support plays an important contribution in the faradaic responses. Decoupling the contribution of the carbon support uncovers that the reactivity of $LaMnO_3$ towards the four-electron ORR pathway is orders of magnitude higher than that for the other lanthanides. We rationalize these observations in terms of changes in the redox state at the B-site close to the formal oxygen reduction potential.

1. Introduction

The oxygen reduction reaction (ORR) is one of the most challenging reactions in energy-conversion devices such as fuel cells and metal–air batteries.[1] In alkaline environments, it is generally considered that the ORR can proceed through a four-electron transfer to produce OH^- [Eq. (1)], or through a two-electron transfer to produce HO_2^- [Eq. (2)]:[2]

$$O_2 + 2\,H_2O + 4\,e^- \rightarrow 4\,OH^- \quad (1)$$

$$O_2 + H_2O + 2\,e^- \rightarrow HO_2^- + OH^- \quad (2)$$

The generation of OH^- from HO_2^- can be achieved by either the redox step [Eq. (3)]:

$$HO_2^- + H_2O + 2\,e^- \rightarrow 3\,OH^- \quad (3)$$

or the decomposition reaction [Eq. (4)]:

$$2\,HO_2^- \rightarrow 2\,OH^- + O_2 \quad (4)$$

Platinum-based catalysts are often quoted as benchmark materials for the ORR in acidic and alkaline environments,[3] but significant efforts have also been focused on earth-abundant and low-cost materials.[4] Noble-metal-based catalysts are fundamentally limited by the so-called *scaling factors* arising from the fact that multiple intermediates are involved in the overall reaction.[5] On the other hand, transition-metal oxides have been generating a lot of interest for fuel cells operating under neutral and high-pH conditions.[6] Complex transition-metal oxides are a huge family of compounds and the establishment of appropriate descriptors linking structure and reactivity is crucially important in this field.

Since the seminal work by Bockris and Otagawa in the 1980s,[7] the establishment of descriptors correlating electronic properties of perovskite oxides and their activities towards oxygen electrocatalysis have been subject of considerable debate. More recently, the elegant work by Suntivich et al.[8b] suggested that single electron occupancy of the e_g orbital represents the optimum configuration for oxygen electrocatalysis.[8] These authors proposed empty e_g orbitals lead to strong B–O_2 bonding, whereas fully occupied e_g orbitals significantly weaken O_2 binding.[8b] DFT calculations also concluded that the adsorption strength of intermediates increases as the number of outer B-site valence electrons increases.[8a,9]

Although these descriptors are conceptually simple and attractive, there are a number of issues that are not fully understood. Discussion mainly focuses on the strength of B–O_2 bonding, which may not necessarily be the rate-determining factor in the four-electron process. Furthermore, recent studies have provided compelling evidence that perovskite-based oxide materials inherently exhibit A-site surface segregation after being prepared at high temperatures.[10] Burriel et al. demonstrated that the outer surface of $La_{2-x}Sr_xNiO_{4+\delta}$ single crystals is mainly (La, Sr)O terminated.[10b]

Another important aspect to consider is that many of these oxides are poor electronic conductors, requiring their disper-

[a] Dr. V. Celorrio, E. Dann, Dr. S. R. Hall, Dr. D. J. Fermin
School of Chemistry, University of Bristol
Cantocks Close, Bristol BS8 1TS (UK)
E-mail: David.Fermin@bristol.ac.uk

[b] Dr. L. Calvillo
Dipartimento di Scienze Chimiche, Università di Padova
Via Marzolo 1, 35131 Padova (Italy)

[c] Dr. D. J. Morgan
Cardiff Catalysis Institute, School of Chemistry
Cardiff University, Cardiff CF10 3AT (UK)

Supporting Information and ORCID(s) from the author(s) for this article are available on the WWW under http://dx.doi.org/10.1002/celc.201500440.

sion in porous carbon films to improve charge transport. As the activity of these oxides is measured in alkaline solution, the contribution of the ORR reaction at the carbon surface (two-electron reaction) must be accounted for.[11] Hardin et al. reported that the addition of carbon to the electrode improved the activity of oxides for oxygen reduction, but not for oxygen evolution, concluding that carbon materials play a key role in the mechanism beyond charge transport.[12] The work by Poux et al. showed that carbon not only offers electrical contact to oxide nanoparticles, but also reduces O_2 to HO_2^-. This process could be coupled to the reaction at the oxide material, which may lead to generation of OH^- by either Equation (3) or (4).[6c,13] Malkhandi et al. observed this synergetic effect, investigating the activity of $La_{0.6}Ca_{0.4}CoO_{3-x}$ (LCCO) supported on acetylene black carbon.[14]

In the present work, we report the analysis of the ORR kinetics catalyzed by phase-pure $LaCrO_3$, $LaMnO_3$, $LaFeO_3$, $LaCoO_3$, and $LaNiO_3$ nanoparticles supported on Vulcan XC-72R. These particles were prepared by using a highly versatile ionic-liquid method.[15] The reactivity of the carbon supported oxides was studied by using rotating ring-disk electrodes (RRDEs), monitoring the ratio between four- and two-electron mechanisms. Employing the model developed by Damjanovic et al.,[16] the phenomenological rate constants for the four-electron process were estimated as a function of the electrode potential. Our studies show that the reactivity of $LaMnO_3$ towards the four-electron process is several orders of magnitude higher than for the other oxides. These observations do not appear to support d-orbital occupancy of the B-site, as the key activity descriptor in these systems. We rationalize the higher activity of $LaMnO_3$ in terms of changes in the oxidation state of Mn^{III} sites at a potential close to the formal ORR potential. We discuss the nature of the active sites and propose an alternative approach to benchmark the reactivity of these materials.

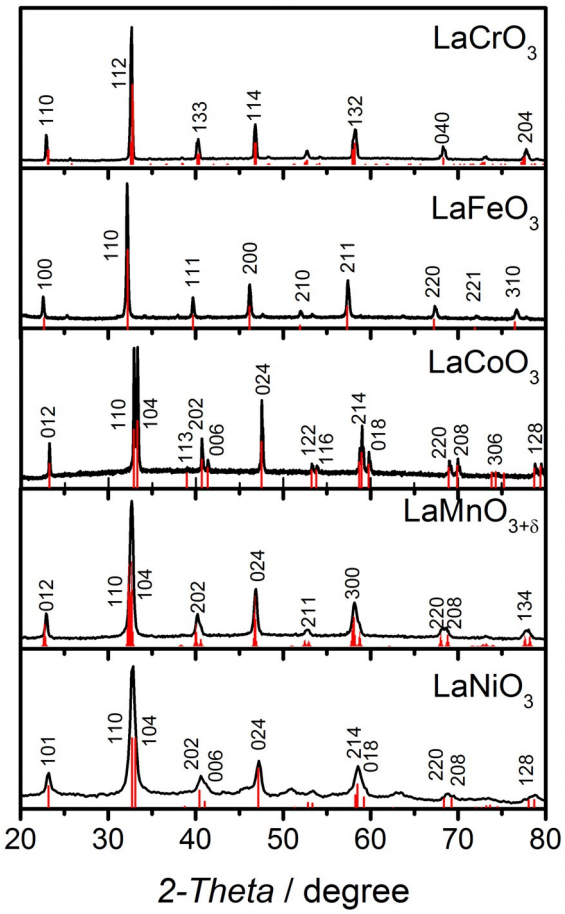

Figure 1. XRD patterns of $LaCrO_3$, $LaFeO_3$, $LaCoO_3$, $LaMnO_{3+\delta}$, and $LaNiO_3$. Red vertical bars correspond to standard patterns, JCPDS-ICDD File Nos. 01-071-1231, 01-075-0541, 00-048-0123, 01-073-8342, and 01-072-1241, respectively.

2. Results and Discussion

Figure 1 shows XRD data of the various oxide nanoparticles synthesized by using the ionic-liquid method. All of the diffractograms are characterized by high phase purities, judging from the match with reported standards. $LaMnO_3$ was indexed to the rhombohedral (*R*-3*cH*) phase, which is consistent with an oxygen excess, δ. Stoichiometric $LaMnO_3$ has been reported to feature an orthorhombic crystal structure,[17] which is characterized by XRD patterns that are substantially different to those shown in Figure 1. A quantitative analysis of the oxygen content based on XRD patterns is somewhat complex, owing to signal broadening introduced by the nanoscale dimensions of the crystalline domains. In the case of $LaMnO_{3+\delta}$, a significant splitting of the XRD peak between 32 and 34° can be observed for values of $\delta > 0.09$. Consequently, we expect oxygen contents below this level for the particles examined in this work. Having established this point, and for the sake of simplicity, we will be referring to this material as $LaMnO_3$ throughout this work. $LaFeO_3$ was indexed to the corresponding cubic (*Pm*3*m*) phase. $LaCrO_3$ exhibited the orthorhombic (*Pbnm*) phase, whereas $LaCoO_3$ and $LaNiO_3$ were assigned to the rhombohedral phase.

A representative SEM image of $LaNiO_3$ is shown in Figure 2, illustrating the characteristic morphology and microstructure of the synthesized oxide. EDX analysis of a section of the porous network reveals a homogeneous distribution of La (Figure 2b) and Ni (Figure 2c) atoms. Quantitative elemental analysis was also consistent with the material stoichiometry. These results, also observed for the other lanthanides (see Figure S1 in the Supporting Information), are consistent with the high phase purity revealed by XRD.

Figures 3a and 3c show representative TEM images of $LaMnO_3$ and $LaNiO_3$, respectively, illustrating nanocrystals with mean particle sizes of 35 nm (TEM images of the other oxides can be found in Figure S2 of the Supporting Information). Particle-size distributions (shown in Figure S3) are relatively broad with $LaMnO_3$, $LaNiO_3$ and $LaCoO_3$ oxides exhibiting a mean diameter between 30 and 35 nm. Larger particles were obtained for $LaFeO_3$ (60 nm) and $LaCrO_3$ (195 nm). The larger particle size for the latter two oxides reflects, to a large extent, the fact that higher temperatures were required to promote phase purity. The lattice fringes observed in high-resolution TEM

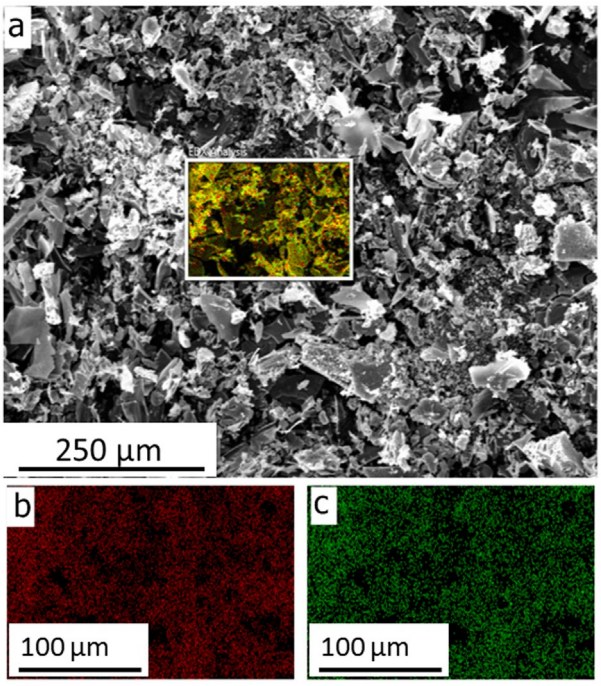

Figure 2. a) Representative SEM images of $LaNiO_3$, with the corresponding b) La and c) Ni elemental mapping.

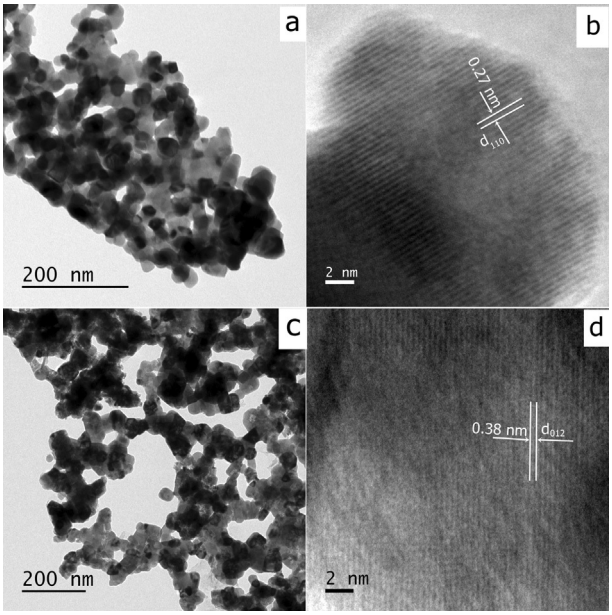

Figure 3. TEM and HRTEM images of as-synthesized $LaMnO_3$ (a, b) and $LaNiO_3$ (c, d).

images (HRTEM) (Figures 3b and 3d) demonstrate the high degree of crystallinity of the as-prepared oxides. The 0.27 nm *d* spacing obtained for $LaMnO_3$ (Figure 3b) is consistent with the {110} planes. Figure 3b also shows that the size of the crystalline domain is comparable to the nanoparticle size. In the case of $LaNiO_3$ (Figure 3d), the 0.38 nm spacing is linked to the {012} planes. HRTEM images of the other oxides can be found in the Supporting Information (Figure S4).

XPS spectra of $LaNiO_3$, $LaMnO_3$, $LaFeO_3$, and $LaCoO_3$ are displayed in Figure 4, showing the La 3d, Ni 2p, Mn 2p, Fe 2p, and Co 2p regions. La $3d_{5/2}$ (833.5–835.1 eV) and La $3d_{3/2}$ (850.3–851.9 eV) signals are split into two peaks, each as a result of contributions from several initial and final states, with the La $3d_{5/2}$ binding energy (BE) consistent with a La^{3+} state.[18] The La 3d line contains also the components associated with La_2O_3/$La(OH)_3$ (components at higher BEs), resulting from La surface segregation,[18c] which may be responsible for slight variations in the peak shape for the various oxides. The La $3d_{3/2}$ peak overlaps with the main Ni $2p_{3/2}$ peak, making the accurate determination of the Ni 2p BE difficult and, therefore, the Ni oxidation state. However, the positions of the Ni $2p_{3/2}$ satellite and Ni $2p_{1/2}$ peaks at 861.4 and 872 eV, respectively, are in agreement with a Ni^{3+} state. The BEs of the Co $2p_{3/2}$ (780.1 eV) and Fe $2p_{3/2}$ (710.2 eV) peaks are also good indicators of the 3+ oxidation state of the B-site. In addition, the Co 2p line does not show the Co $2p_{3/2}$ satellite peak at 786 eV, characteristic of Co^{2+}. The presence of a Fe $2p_{3/2}$ satellite peak at 719 eV further supports the assignment to a Fe^{3+} oxidation state. In the case of Mn $2p_{3/2}$, the BEs associated with the oxidation states 4+ (642.2 eV) and 3+ (641.9 eV) are very difficult to resolve. However, taking into account the information obtained from XRD, electron microscopy, and elemental analysis, we can conclude that the B-site oxidation state of all of the as-grown material is primarily +3.

La/B-site surface atomic ratios in the range of 2–5 were observed for this family of lanthanides, indicating a significant surface segregation of the A-site. Observations of La-enriched surfaces are consistent with previous reports on other perovskite materials.[10a,b] This is rather significant in the case of $LaCoO_3$, which is responsible for the low signal-to-noise-ratio of the Co 2p photoemission lines. Although the ensemble of characterization studies consistently show high phase purity and crystallinity, the observation of La-enriched surfaces may call into question the role of the B-site on the electrocatalytic properties of these materials.

Figure 5 compares the current densities at the disk (j_D, bottom panel) and the ring (j_R, top panel) of $LaCrO_3$, $LaMnO_3$, $LaFeO_3$, $LaCoO_3$, and $LaNiO_3$ electrodes at 1600 rpm and 0.010 V s^{-1} in a O_2-saturated 0.1 M KOH solution. Current densities were calculated by using the electrode geometrical area. Under the same conditions, the responses obtained for Pt/Etek and a Vulcan film are also shown. The onset potential for 20 wt% Pt/Etek catalysts is in agreement with previous studies in the literature.[19] The first striking observation is that the onset potential for the ORR is similar for several oxides and the Vulcan film. This onset potential falls within the range of values reported in the literature for various carbon materials in alkaline media.[20] On the other hand, $LaMnO_3$ shows an onset potential significantly more positive, featuring a shoulder in the range of 0.75–0.85 V. As discussed further below, this feature is important in order to understand the high activity of $LaMnO_3$. The response observed for the Pt-based catalyst is consistent with the $4e^-$ ORR pathway.[21] The angular rotation rate affects the overall current density in large portions of the potential range, as illustrated for $LaMnO_3$, $LaNiO_3$, and Vulcan

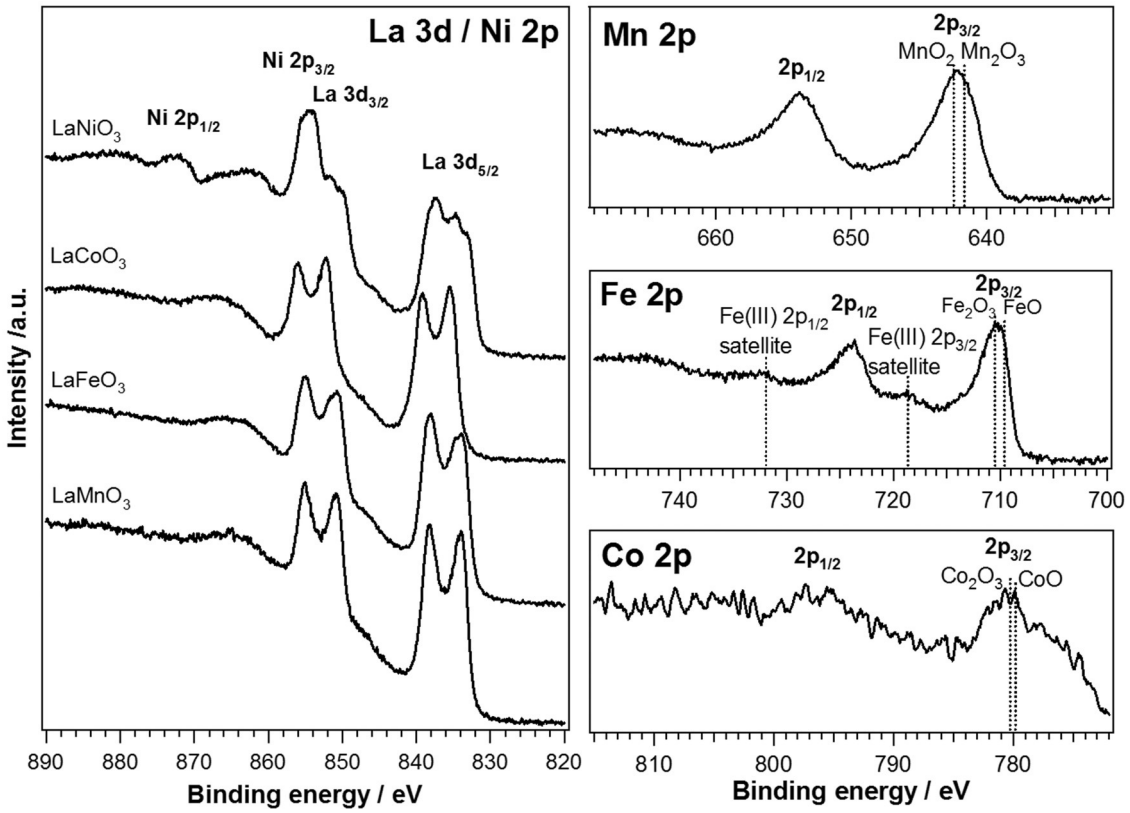

Figure 4. Characteristic XPS spectra of La 3d, Ni 2p, Mn 2p, Fe 2p, and Co 2p core levels for $LaNiO_3$, $LaMnO_3$, $LaFeO_3$,and $LaCoO_3$.

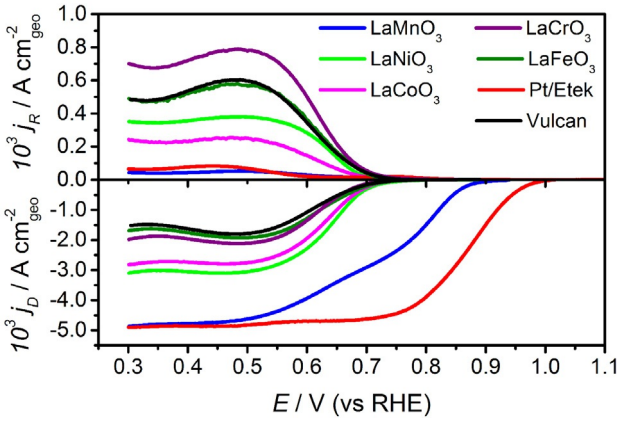

Figure 5. Disk current density (j_D) as a function of potential of Vulcan-supported $LaCrO_3$, $LaMnO_3$, $LaFeO_3$, $LaCoO_3$, and $LaNiO_3$ electrodes at 1600 rpm in O_2-saturated 0.1 M KOH and a scan rate of 10 mV s^{-1}. The Pt ring responses (j_R) were recorded by holding the potential at +1.1 V. The performance of the lanthanide catalysts are also contrasted with those of the carbon support (Vulcan) and the commercial Pt/Etek catalyst.

electrodes (no oxide catalysts) in the Supporting Information (Figures S5 and S6).

It is interesting to see that the magnitude of the ring and disk current densities for $LaCrO_3$, $LaFeO_3$, and $LaNiO_3$ electrodes are affected by the nature of the B-site. However, the ORR onset potential is very similar for all of these materials and close to the onset potential for the Vulcan film. This behavior is consistent with the view that B-site plays a role in the catalytic activity of the ORR, but primarily on the reduction of HO_2^- [Eqs. (3) and (4)].[22] The catalytic activity of perovskite materials in the HO_2^- disproportionation reaction has been discussed in previous publications.[13a,23]

By using the current values recorded at the disk and ring electrodes at 1600 rpm, the HO_2^- yield was calculated as function of the electrode potential for each of the materials investigated (Figure S7). $LaMnO_3$ and Pt/Etek electrodes exhibit less than 7% HO_2^- yield over the entire potential range, whereas the other perovskites exhibit a more substantial yield, following the trend $LaCrO_3 > LaFeO_3 > LaNiO_3 > LaCoO_3$. This behavior shows that $LaMnO_3$ not only features a significantly more positive onset potential for the ORR, but also a stronger tendency to the $4e^-$ process [Eq. (1)]. As shown in Figure S8, decreasing the $LaMnO_3$ loading to 62.5 μg cm^{-2} leads to a slight increase in the ring current density and a decrease in the diffusion-limited disk current density. This behavior is expected, as the overall contribution of the carbon support to the ORR increases with decreasing catalyst loading. However, in the potential range where the ORR exclusively takes place at the $LaMnO_3$ particles (between 0.7 and 0.9 V), the ring current remains low and independent of the oxide loading. This observation confirms that low HO_2^- yields in the presence of $LaMnO_3$ are not related to catalyst loading.

Figure 6 exemplifies the dependence of the disk current (i_D) on the angular rotation (ω) for $LaMnO_3$ and $LaNiO_3$, following the Koutecky–Levich formalism [Eq. (5)]:

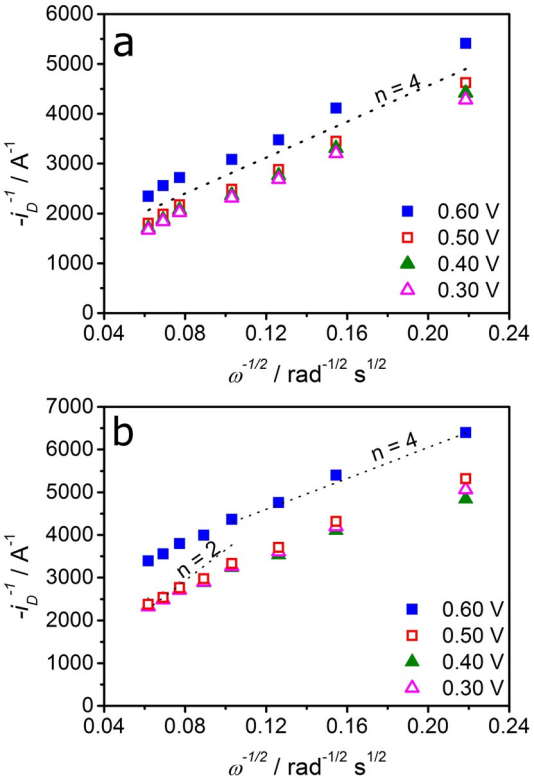

Figure 6. Koutecky–Levich plots for the ORR on a) $LaMnO_3$ and b) $LaNiO_3$ electrodes in O_2-saturated 0.1 M KOH at different potentials. Dotted lines represent the characteristic slopes for the two different reactions.

$$\frac{1}{i_D} = \frac{1}{i_k} + \frac{1}{i_L} = \frac{1}{i_k} + \frac{1}{0.62nAFcD^{2/3}\nu^{-1/6}\omega^{1/2}} \quad (5)$$

where i_k and i_L are the kinetically and mass-transport limiting current. The latter parameter is dependent on the number of transferred electrons (n), oxygen diffusion coefficient ($D = 1.9 \times 10^{-5}$ cm^2 s^{-1}),[24] bulk oxygen concentration ($c = 1.2 \times 10^{-6}$ mol cm^3), and kinematic viscosity ($\nu = 0.01$ cm^2 s^{-1}). Other parameters in Equation (5) include the disk geometric area (A) and the Faraday constant (F). $LaMnO_3$ (Figure 6a) exhibits a linear dependence in the potential range between 0.60 and 0.30 V, with a slope consistent with $n = 4$. The same slope can also be observed at potentials close to 0.9 V and for a $LaMnO_3$ loading as low as 62.5 μg cm^{-2} (Figure S8). On the other hand, $LaNiO_3$ (Figure 6b) shows a slight change in slope with increasing angular rotation rate, which is also seen for $LaCrO_3$, $LaFeO_3$, and $LaCoO_3$ (Figure S9). The change in slope can be linked to the dynamics of peroxide reduction at the catalyst surface, considering a reaction path based on Equations (2) and (3). Increasing rotation rates can decrease the probability of the second reduction step [Eq. (3)], leading to a value of n that is closer to 2. Figure S10 shows the effective value of n, as estimated from the ratio between the ring and disk currents at 1600 rpm, evolving from values between 2 and 3 for the various oxides to a value of 4 for $LaMnO_3$ and Pt.

Several models have been developed for quantitative analysis of ORR kinetics employing RRDEs.[16,25] One of the simplest approaches was proposed by Damjanovic et al., correlating the ring and disk currents to establish the ORR pathway.[16] As illustrated in Scheme 1, the direct 4e$^-$ oxygen reduction pathway is defined in terms of negligible population of HO_2^- within the experimental timescale. On the other hand, the so-called indirect path involves a measurable population of HO_2^-, which can be detected at the ring. In Scheme 1, only species within the reaction layer (denoted with *) can undergo electron transfer with either the disk or the ring, as opposed to bulk (b) species.

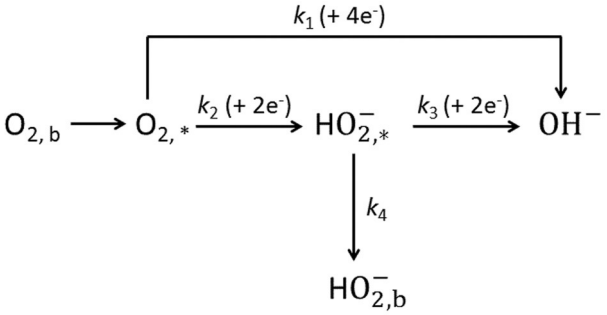

Scheme 1. Simplified ORR mechanism, illustrating the direct and indirect pathways with the associated phenomenological rate constants k_1, k_2, and k_3. Subscripts b and * designate bulk and reaction layer, respectively.

The phenomenological rate constants associated with direct (k_1) and indirect (k_2) pathways contain contributions from a variety of parameters such as particle size, catalyst loading, intermediate coverage, rate constant of elementary electron-transfer steps, and so forth. Full details on the assessment of the various rate constants are given in the Supporting Information [Eqs. (S3)–(S9)]. We focus on the value of k_1, as this is the relevant parameter in the context of alkaline fuel cell applications. As described in the Supporting Information, k_1 is directly extracted from the values of i_D, i_R, and N.

Figure 7a shows the potential dependence of k_1 for the various lanthanides. The phenomenological rate constants show an exponential increase as the potential decreases, with $LaMnO_3$ exhibiting measurable values at potentials more than 150 mV more positive than the other lanthanides. The potential dependence of this rate constant is similar for all oxides. Extrapolating the value of k_1 to 0.7 V allows a comparison of the various oxides to be established, as exemplified in Figure 7b. We have chosen this potential to minimize extrapolation of the measure trends over large potential ranges. Figure 7b further emphasizes the fact that $LaMnO_3$ exhibits a unique activity towards the ORR. Indeed, small differences in the overall magnitude of k_1 can be observed for the Fe-, Co-, and Ni-based oxides, whereas $LaCrO_3$ exhibits significantly lower values. The ratio of k_2/k_1 is shown in Figure S11 of the Supporting Information. The trend is the opposite of that observed for k_1, with $LaCrO_3$ exhibiting a ratio three orders of magnitude higher than $LaMnO_3$. On the other hand, the values for the phenomenological k_3 constant were in the range of 10^{-3} to 10^{-4} cm s^{-1} for all oxides over the potential range investigated (Figure S11).

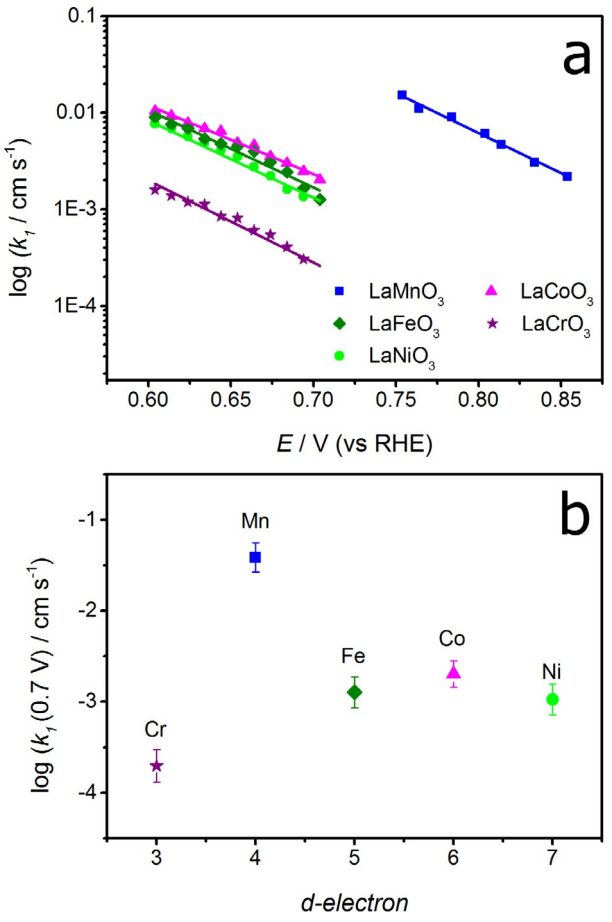

Figure 7. a) Phenomenological rate constant for the direct 4 e$^-$ process (k_1) calculated for the different materials in 0.1 M KOH employing Damjanovic's method. b) k_1 at 0.7 V versus the number of d electrons in the B-site metal. As the ORR onset potential is very different in the case of $LaMnO_3$, the value of k_1(0.7 V) was obtained by extrapolating the trend in Figure 7a. These plots demonstrate that the reactivity of $LaMnO_3$ towards the 4 e$^-$ ORR is significantly higher, which cannot be directly correlated to B-site orbital occupancy.

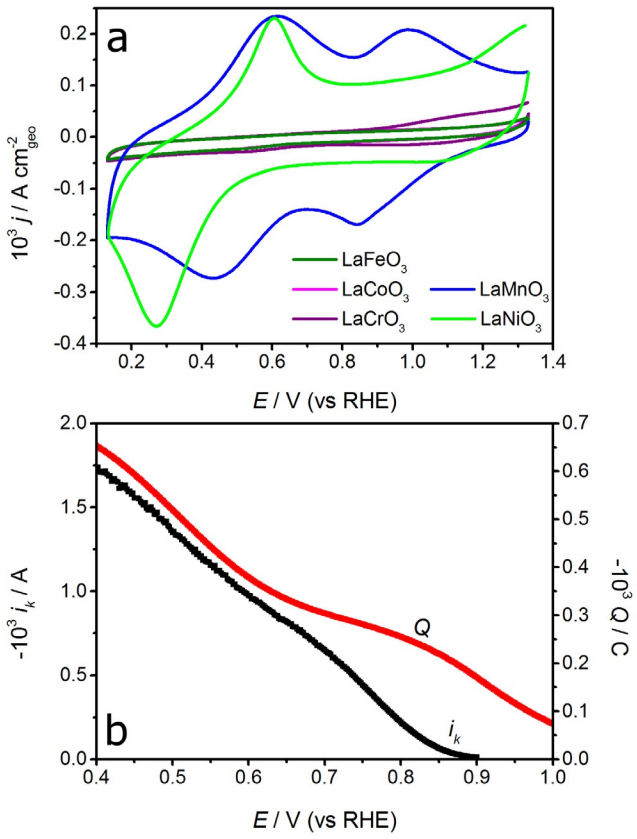

Figure 8. a) Cyclic voltammograms of the Vulcan-supported oxides in Ar-saturated 0.1 M KOH solution at 10 mV s^{-1}. Oxide loading is identical to those reported in Figure 5. The responses of $LaCoO_3$ and $LaCrO_3$ are superimposed and cannot be clearly differentiated in this scale. b) Potential dependence of i_k and the charge associated with redox processes at $LaMnO_3$.

As shown in Figure 7b, the value of k_1 does not correlate with the number of d electrons of the B-site. Furthermore, the single e_g orbital occupancy descriptor fails to describe this trend.[8b] $LaFeO_3$ has double e_g occupancy, whereas $LaCoO_3$, $LaNiO_3$, and $LaMnO_3$ have single occupancy, and $LaCrO_3$ exhibits empty e_g orbitals.[8a,26] It could be argued that the vacant e_g orbitals in $LaCrO_3$ determine the low performance of this material for direct ORR, yet it is clear that the high activity of $LaMnO_3$ arises from an entirely different physical parameter. To rationalize this activity trend, we focus our attention on the redox properties of the perovskite oxides in the absence of O_2.

Figure 8a contrasts cyclic voltammograms of the various Vulcan-supported oxides in argon-saturated 0.1 M KOH solution at 10 mV s^{-1}. No clear redox responses can be observed for $LaFeO_3$, $LaCoO_3$, or $LaCrO_3$ within the potential window relevant to the ORR reaction. $LaNiO_3$ does exhibit a reduction wave with an onset located around 0.2 V more negative than the onset of the ORR at the carbon support. Figure 8a also shows that $LaMnO_3$ exhibits two reduction steps with peaks centered at 0.90 and 0.45 V. These changes in oxidation state occur in the same potential range reported for the reduction of Mn_2O_3 to Mn_3O_4 and from Mn_3O_4 to $Mn(OH)^+$, respectively.[19c,27] It can be seen that only $LaMnO_3$ clearly exhibits changes in redox states at potentials more positive than the onset of the ORR at the carbon support. Consequently, we postulate that the higher activity with respect to other lanthanides is directly linked to changes in Mn oxidation state close to the ORR formal redox potential.

The charge associated with the reduction steps at $LaMnO_3$ as a function of the applied potential is displayed in Figure 8b. On average, the charge obtained across the potential range is consistent with approximately 2% of the Mn population per nanoparticle undergoing an oxidation state change for Mn^{3+} to Mn^{2+}. However, integration of these voltammetric responses is somewhat complicated by the presence of a large capacitive current, which is also observed in the case of $LaNiO_3$. This interesting observation has already been reported by Stevenson and co-workers, linking this phenomenon to anion (OH^-) intercalation.[28] Figure S11 graphically exemplifies the background subtraction implemented for estimating the reduction charge. It should also be mentioned that the faradaic charges associated with the anodic and cathodic cycles are very similar, whereas the responses appear stable within a number of cycles in

this potential range. These results suggest that the stability of these materials is not significantly compromised within the timescale of these experiments.

Figure 8b also shows the change in the kinetically limited current (i_k) obtained from Koutecky–Levich analysis of the $LaMnO_3$. Interestingly, the reduction charge and i_k show similar trends as a function of the applied potential, except at values more positive than 0.9 V. There is a sizeable increase in the charge at potentials above 0.9 V, which does not manifest itself in clear changes in i_k. It should be considered that a variety of processes can be contributing to the electrochemical responses in this potential range, as recently reviewed by Shao-Horn and co-workers, highlighting aspects related to crystallite size and phases.[29] Ahmad et al. estimated differences in O_2 BEs as large as 2 eV for different Mn sites as a result of Jahn–Teller distortions in orthorhombic phases.[30] Furthermore, processes such as OH^- intercalation, mentioned above,[28] may also contribute to the current responses in this potential range. Consequently, additional studies are required to rationalize the various processes contributing to the voltammetric responses and to identify the species responsible for the strong changes in i_k.

Finally, an interesting point to assess is the performance of $LaMnO_3$ with respect to Pt/Etek, considering that both materials essentially operate through the $4e^-$ reduction mechanism. Table S2 summarizes the main activity descriptors obtained from the RRDE responses, including i_k at 0.90 V. This parameter is commonly used as an activity descriptor, avoiding controversial extrapolations over large potential ranges (Tafel plots).[21c] Table S2 shows values of $(2.4\pm0.4)\cdot10^{-4}$ and $(1.2\pm0.2)\cdot10^{-5}$ A for Pt and $LaMnO_3$ catalysts, respectively, which reflect the difference in the current–potential relationship between Pt/Etek and $LaMnO_3$ seen in Figure 5. However, it should be considered that the catalyst loadings and particle sizes are significantly different for both materials (see Table S1 in the Supporting information). Normalizing i_k(0.90 V) by the specific surface area (SSA) [the SSA was calculated by assuming that the oxide particles are spherical, using the ratio $SSA\,(m^2\,g^{-1})=6\times10^3/\rho d$, where ρ is the density of the particle and d is the diameter], we estimate $(8.0\pm1.4)\cdot10^{-6}\,A\,cm^{-2}$ for Pt and $(1.5\pm0.1)\cdot10^{-6}\,A\,cm^{-2}$ for $LaMnO_3$ (see Table S2). The value obtained for Pt/Etek is consistent with values reported in the literature under alkaline conditions.[21a,c] On the other hand, we obtained kinetic currents normalized by mass that were comparable to recent reports.[27b,29] In this analysis, it ought to be considered that significant levels of A-site segregation can occur in this material, according to our XPS analysis as well as by others.[31] The charge estimated from the voltammetric responses (see Figures 8b and S11) over the entire potential range can be used as an indication of the number density of surface Mn sites. In the case of Pt nanostructures, the number density of surface Pt atoms can be estimated from voltammetric parameters such as hydrogen desorption, oxide reduction, and adsorbed CO oxidation peaks (see Figure S11). Normalizing the kinetic current at 0.90 V by the number of electroactive surface sites, we obtain values on the order of $(2.9\pm0.3)\cdot10^{-21}$ and $(1.3\pm0.4)\cdot10^{-20}$ A for $LaMnO_3$ and Pt-Etek, respectively. The error margins in these estimations also take into account uncertainty in the background subtraction. This analysis reveals that surface Mn^{III} sites are significantly more active than previously considered, in particular if kinetic descriptors are normalized only by mass or SSA.

The ensemble of experimental observations strongly indicates that changes in the oxidation state of Mn^{III} sites are a key process leading to the ORR, including oxygen bond breaking. We believe that these observations are crucially important for rationalizing the properties of these materials. Parameters such as oxygen adsorption energies at surfaces in their equilibrium electronic configuration only represent one aspect of the physics involved in these complex reactions. In the broader context of oxygen electrocatalysis, these results are also consistent with recent studies showing that the most active catalysts for the oxygen evolution reaction exhibit changes in redox states under operational conditions.[32] The challenge remains to identify the most active Mn sites and to develop synthetic routes to overexpress these sites. For example, selecting the appropriate A-site may not only lead to an optimum charge density at the Mn sites,[33] but also minimize its surface depletion.

3. Conclusions

We have shown that $LaMnO_3$ exhibits unique activity towards the ORR, which is linked to changes in oxidation state of the B-cation at potentials close to the formal oxygen redox potential. Our investigations revealed that descriptors such as the number of d electrons or the e_g orbital occupancy cannot rationalize the several orders of magnitude difference in activity between $LaMnO_3$ and several other lanthanides towards the $4e^-$ reduction mechanism. To uncover this piece of information, quantitative electrochemical studies involving rotating ring-disk electrodes were performed to deconvolute the reaction pathways and to quantify their corresponding rate constants. Furthermore, quantitative analysis was enabled by the preparation of Vulcan-supported oxides with high phase purity, crystallinity, and nanoscale structures. Indeed, our versatile ionic-liquid-based approach allowed the facile synthesis of $LaCrO_3$, $LaMnO_3$, $LaFeO_3$, $LaCoO_3$, and $LaNiO_3$.

We provide conclusive evidence, confirming that carbon supports play a major role in the ORR process, particularly in the case of $LaCrO_3$, $LaFeO_3$, $LaCoO_3$, and $LaNiO_3$. The ORR onset potential at these oxides overlaps with HO_2^- generation at the carbon support. On the other hand, $LaMnO_3$ exhibited an onset potential for the ORR that was significantly more positive than the other carbon-supported oxides, with nearly 100% selectivity towards the $4e^-$ reaction. This behavior translates into a phenomenological electron rate constant for the $4e^-$ process several orders of magnitude higher in the case of $LaMnO_3$. The origin of this distinctive reactivity is associated with the electronic population of Mn^{III} surface state with energy closely overlapping with the oxygen reduction energy. A key challenge is to identify the nature of the active Mn^{III} state in order to develop synthetic methods capable of overexpressing this active site. Other results, to be reported elsewhere, show that this site can be affected by the oxygen content in the crystal structure as well as the properties of the A-site.

Experimental Section

$LaCrO_3$, $LaMnO_3$, $LaFeO_3$, $LaCoO_3$, and $LaNiO_3$ particles were synthesized by using an ionic liquid/cellulose system based on a procedure reported elsewhere.[15] Briefly, a 1 M aqueous solution of the metal precursors (nitrate salts) (1 mL) was added to a vial containing 1-ethyl-3-methylimiamidizolium acetate (1 mL) and heated at 80 °C for 2 h to promote water evaporation and precursor phase transfer. Dissolution of cellulose (100 mg), acting as a chelating agent, over the course of 15 min and subsequent calcination of the mixture at different temperatures for 2 h produced the desired multicomponent metal-oxide phase. The calcination temperature was set at 700 °C for $LaMnO_3$, 800 °C for $LaNiO_3$ and $LaCoO_3$, and 900 °C for $LaFeO_3$ and $LaCrO_3$. The different calcination temperatures were established such that high levels of crystallinity are ensured, while minimizing the presence of secondary phases. Phase purity is the key parameter to control, requiring the crystallization temperature to be adjusted according to the thermochemistry of the B-precursor.

XRD was performed with a Bruker AXS D8 Advance diffractometer featuring a CuKα radiation source ($\lambda = 0.154$ nm). X-ray photoelectron spectra (XPS) were acquired with a Kratos Ultra Axis XPS system equipped with a delay-line detector (DLD). Core-level photoemission spectra were taken at room temperature in normal emission by using a monochromatic AlKα X-ray source (1486.7 eV). Single spectral regions were collected by using 0.1 eV steps, a 0.5 s collection time, and 20 eV pass energy. The BEs were referenced to the C 1s peak at 284.7 eV (not shown). The structure of the catalyst was also investigated with scanning (JEOL SEM 5600 LV) and transmission electron microscopy (JEOL JEM-1400Plus and JEOL JEM 2010). Samples for TEM were produced by placing 1 μL drops of the oxide particles dissolved in ethanol on a 3 mm diameter carbon-coated copper grid. Mean particle diameters were estimated from at least 100 nanoparticles per sample.

Electrochemical measurements were conducted by using a rotating ring-disk electrode (RRDE) operated with an ALS Rotation Controller and an Ivium-CompactStat bipotentiostat. The RRDE consisted of a 4 mm diameter glassy carbon disk and a platinum ring with a 7 mm outer diameter. The RRDE collection efficiency was determined to be 0.42, employing ferrocene methanol as the redox probe. Pt foil and Hg/HgO (1 M NaOH, IJ Cambria) were used as counter and reference electrodes, respectively. We performed experiments with different counter electrodes, including graphite and Au rods, confirming that the responses are not affected by contamination from the counter electrode (see Figure S12 in the Supporting Information). Furthermore, there was no time dependence in the performance of any of the catalysts, which may suggest any aging issues within the timescale of the studies. Each set of experiments was carried out with fresh electrolyte solution. The reference electrode, which was calibrated against the reversible hydrogen electrode (RHE), was placed in a separate compartment and connected by a Luggin capillary. To facilitate the discussion, all potentials herein are quoted against the RHE. Measurements were carried out in a 0.1 M KOH solution purged either with high-purity Ar or O_2 (BOC). The uncompensated resistance estimated by electrochemical impedance spectroscopy was typically 70 Ω. Under the current experimental conditions, effects from *IR* compensation were negligible.

Electrodes were prepared by using a two-step drop-casting process. Controlled amounts of an ink containing Vulcan and Na^+-exchanged Nafion (5 wt%, Sigma–Aldrich) were deposited onto the glassy carbon disk, followed by drop-casting an aqueous suspension of the oxide. Keeping the oxide and carbon in separate suspensions allows the homogeneity of the suspensions to be visualized prior to the drop-casting steps. The final loading on each electrode was 250 $\mu g_{oxide}\,cm^{-2}$, 50 $\mu g_{Vulcan}\,cm^{-2}$, and 50 $\mu g_{Nafion}\,cm^{-2}$. This catalyst loading is comparable to other works in the literature.[6b,34] This leads to an effective Nafion film thickness of less than 0.5 μm [calculated as $\tau = m/(\pi r^2 \rho)$, where m is the mass of Nafion at the electrode and is ρ the film density, which can be assumed to be 2.0 $g\,cm^{-3}$]. Such thin Nafion layers ensure that any potential film diffusion resistance remain negligible.[21a,35] Finally, 20 wt% Pt supported on Vulcan XC-72 (Pt/Etek) was used as a benchmark in these studies. The loading of the catalysts at the electrode surface was 250 $\mu g_{Pt}\,cm^{-2}$, 1000 $\mu g_{carbon}\,cm^{-2}$, and 50 $\mu g_{Nafion}\,cm^{-2}$. We performed a large number of experiments employing $LaMnO_3$, with different catalyst loadings, to confirm the reproducibility and self-consistency of our approach (see Figure S8 in the Supporting Information). Values reported here were obtained from averaging the responses of 3–6 different catalysts layer of each material prepared on different days.

Acknowledgements

V.C. gratefully acknowledges the Royal Society and the UK National Academy for support through the Newton International Fellows program. SEM/EDX studies were carried out by the Chemical Imaging Facility, University of Bristol (UoB) with equipment funded by the EPSRC under Grant "Atoms to Applications" Grant ref. "(EP/K035746/1). TEM studies were carried out in the Chemistry Imaging Facility at UoB with equipment funded by UoB and EPSRC (EP/K035746/1 and EP/M028216/1).

Keywords: carbon support · electrocatalysis · $LaMnO_3$ · oxygen reduction reaction · perovskite nanoparticles

[1] S. Park, Y. Shao, J. Liu, Y. Wang, *Energy Environ. Sci.* **2012**, *5*, 9331–9344.
[2] C. Song, J. Zhang, in *PEM Fuel Cell Electrocatalysts and Catalyst Layers* (Ed.: J. Zhang), Springer, London, **2008**, pp. 89–134.
[3] N. M. Marković, T. J. Schmidt, V. Stamenković, P. N. Ross, *Fuel Cells* **2001**, *1*, 105–116.
[4] a) B. Wang, *J. Power Sources* **2005**, *152*, 1–15; b) F. Jaouen, E. Proietti, M. Lefevre, R. Chenitz, J.-P. Dodelet, G. Wu, H. T. Chung, C. M. Johnston, P. Zelenay, *Energy Environ. Sci.* **2011**, *4*, 114–130; c) Z. Chen, D. Higgins, A. Yu, L. Zhang, J. Zhang, *Energy Environ. Sci.* **2011**, *4*, 3167–3192.
[5] a) J. Greeley, I. E. L. Stephens, A. S. Bondarenko, T. P. Johansson, H. A. Hansen, T. F. Jaramillo, J. Rossmeisl, I. Chorkendorff, J. K. Nørskov, *Nat. Chem.* **2009**, *1*, 552–556; b) J. Rossmeisl, A. Logadottir, J. K. Nørskov, *Chem. Phys.* **2005**, *319*, 178–184.
[6] a) J. Sunarso, A. A. J. Torriero, W. Zhou, P. C. Howlett, M. Forsyth, *J. Phys. Chem. C* **2012**, *116*, 5827–5834; b) J. Suntivich, H. A. Gasteiger, N. Yabuuchi, Y. Shao-Horn, *J. Electrochem. Soc.* **2010**, *157*, B1263–B1268; c) T. Poux, F. S. Napolskiy, T. Dintzer, G. Kéranguéven, S. Y. Istomin, G. A. Tsirlina, E. V. Antipov, E. R. Savinova, *Catal. Today* **2012**, *189*, 83–92.
[7] J. O. M. Bockris, T. Otagawa, *J. Electrochem. Soc.* **1984**, *131*, 290–302.
[8] a) Y. Wang, H.-P. Cheng, *J. Phys. Chem. C* **2013**, *117*, 2106–2112; b) J. Suntivich, H. A. Gasteiger, N. Yabuuchi, H. Nakanishi, J. B. Goodenough, Y. Shao-Horn, *Nat. Chem.* **2011**, *3*, 647–651; c) Y.-L. Lee, J. Kleis, J. Rossmeisl, Y. Shao-Horn, D. Morgan, *Energy Environ. Sci.* **2011**, *4*, 3966–3970.
[9] F. Calle-Vallejo, N. G. Inoglu, H.-Y. Su, J. I. Martinez, I. C. Man, M. T. M. Koper, J. R. Kitchin, J. Rossmeisl, *Chem. Sci.* **2013**, *4*, 1245–1249.
[10] a) J. Druce, H. Tellez, M. Burriel, M. D. Sharp, L. J. Fawcett, S. N. Cook, D. S. McPhail, T. Ishihara, H. H. Brongersma, J. A. Kilner, *Energy Environ. Sci.* **2014**, *7*, 3593–3599; b) M. Burriel, S. Wilkins, J. P. Hill, M. A. Munoz-Marquez, H. H. Brongersma, J. A. Kilner, M. P. Ryan, S. J. Skinner, *Energy Environ. Sci.* **2014**, *7*, 311–316; c) J. A. Kilner, M. Burriel, *Annu. Rev.*

Mater. Res. **2014**, *44*, 365 – 393; d) H. Téllez, J. Druce, Y.-W. Ju, J. Kilner, T. Ishihara, *Int. J. Hydrogen Energy* **2014**, *39*, 20856 – 20863; e) M. L. Reinle-Schmitt, C. Cancellieri, A. Cavallaro, G. F. Harrington, S. J. Leake, E. Pomjakushina, J. A. Kilner, P. R. Willmott, *Nanoscale* **2014**, *6*, 2598 – 2602; f) J. Chen, M. Döbeli, D. Stender, K. Conder, A. Wokaun, C. W. Schneider, T. Lippert, *Appl. Phys. Lett.* **2014**, *105*, 114104.

[11] a) M. Appel, A. J. Appleby, *Electrochim. Acta* **1978**, *23*, 1243 – 1246; b) D.-W. Wang, D. Su, *Energy Environ. Sci.* **2014**, *7*, 576 – 591.

[12] a) W. G. Hardin, D. A. Slanac, X. Wang, S. Dai, K. P. Johnston, K. J. Stevenson, *J. Phys. Chem. Lett.* **2013**, *4*, 1254 – 1259; b) W. G. Hardin, J. T. Mefford, D. A. Slanac, B. B. Patel, X. Wang, S. Dai, X. Zhao, R. S. Ruoff, K. P. Johnston, K. J. Stevenson, *Chem. Mater.* **2014**, *26*, 3368 – 3376.

[13] a) T. Poux, A. Bonnefont, A. Ryabova, G. Kerangueven, G. A. Tsirlina, E. R. Savinova, *Phys. Chem. Chem. Phys.* **2014**, *16*, 13595 – 13600; b) T. Poux, A. Bonnefont, G. Kéranguéven, G. A. Tsirlina, E. R. Savinova, *ChemPhysChem* **2014**, *15*, 2108 – 2120.

[14] S. Malkhandi, P. Trinh, A. K. Manohar, K. C. Jayachandrababu, A. Kindler, G. K. Surya Prakash, S. R. Narayanan, *J. Electrochem. Soc.* **2013**, *160*, F943 – F952.

[15] a) V. Celorrio, K. Bradley, O. J. Weber, S. R. Hall, D. J. Fermín, *ChemElectroChem.* **2014**, *1*, 1667 – 1671; b) D. C. Green, S. Glatzel, A. M. Collins, A. J. Patil, S. R. Hall, *Adv. Mater.* **2012**, *24*, 5767 – 5772.

[16] A. Damjanovic, M. A. Genshaw, J. O. Bockris, *J. Chem. Phys.* **1966**, *45*, 4057 – 4059.

[17] J. Rodríguez-Carvajal, M. Hennion, F. Moussa, A. H. Moudden, L. Pinsard, A. Revcolevschi, *Phys. Rev. B* **1998**, *57*, R3189 – R3192.

[18] a) M. F. Sunding, K. Hadidi, S. Diplas, O. M. Løvvik, T. E. Norby, A. E. Gunnæs, *J. Electron Spectrosc. Relat. Phenom.* **2011**, *184*, 399 – 409; b) M. C. Álvarez-Galván, V. A. de La Peña O'Shea, G. Arzamendi, B. Pawelec, L. M. Gandía, J. L. G. Fierro, *Appl. Catal. B* **2009**, *92*, 445 – 453; c) K. Bolwin, W. Schnurnberger, G. Schiller, *Z. Phys. B* **1988**, *72*, 203 – 209.

[19] a) Y. Gorlin, T. F. Jaramillo, *J. Am. Chem. Soc.* **2010**, *132*, 13612 – 13614; b) Y. Gorlin, C.-J. Chung, D. Nordlund, B. M. Clemens, T. F. Jaramillo, *ACS Catal.* **2012**, *2*, 2687 – 2694; c) H.-Y. Su, Y. Gorlin, I. C. Man, F. Calle-Vallejo, J. K. Norskov, T. F. Jaramillo, J. Rossmeisl, *Phys. Chem. Chem. Phys.* **2012**, *14*, 14010 – 14022.

[20] a) G. Zhutaeva, V. Bogdanovskaya, E. Davydova, L. Kazanskii, M. Tarasevich, *J. Solid State Electrochem.* **2014**, *18*, 1319 – 1334; b) K. Tammeveski, K. Kontturi, R. J. Nichols, R. J. Potter, D. J. Schiffrin, *J. Electroanal. Chem.* **2001**, *515*, 101 – 112.

[21] a) U. A. Paulus, T. J. Schmidt, H. A. Gasteiger, R. J. Behm, *J. Electroanal. Chem.* **2001**, *495*, 134 – 145; b) T. J. Schmidt, V. Stamenkovic, J. P. N. Ross, N. M. Markovic, *Phys. Chem. Chem. Phys.* **2003**, *5*, 400 – 406; c) H. A. Gasteiger, S. S. Kocha, B. Sompalli, F. T. Wagner, *Appl. Catal. B* **2005**, *56*, 9 – 35.

[22] F. d. r. Jaouen, *J. Phys. Chem. C* **2009**, *113*, 15433 – 15443.

[23] a) Y. N. Lee, R. M. Lago, J. L. G. Fierro, J. González, *Appl. Catal. A* **2001**, *215*, 245 – 256; b) H. Falcón, R. E. Carbonio, J. L. G. Fierro, *J. Catal.* **2001**, *203*, 264 – 272; c) A. Ariafard, H. R. Aghabozorg, F. Salehirad, *Catal. Commun.* **2003**, *4*, 561 – 566.

[24] A. J. Bard, L. R. Faulkner, *Electrochemical methods : fundamentals and applications*, John Wiley & Sons, New York, NY, **1980**.

[25] a) H. S. Wroblowa, P. Yen Chi, G. Razumney, *J. Electroanal. Chem.* **1976**, *69*, 195 – 201; b) A. J. Appleby, M. Savy, *J. Electroanal. Chem.* **1978**, *92*, 15 – 30; c) R. W. Zurilla, R. K. Sen, E. Yeager, *J. Electrochem. Soc.* **1978**, *125*, 1103 – 1109; d) V. S. Bagotzky, N. A. Shumilova, G. P. Samoilov, E. I. Khrushcheva, *Electrochim. Acta* **1972**, *17*, 1625 – 1635; e) N. A. Anastasijević, V. Vesović, R. R. Adžić, *J. Electroanal. Chem.* **1987**, *229*, 305 – 316.

[26] a) B. W. Veal, D. J. Lam, *J. Appl. Phys.* **1978**, *49*, 1461 – 1462; b) U. Maitra, B. S. Naidu, A. Govindaraj, C. N. R. Rao, *Proc. Natl. Acad. Sci. USA* **2013**.

[27] a) M. Wiechen, H.-M. Berends, P. Kurz, *Dalton Trans.* **2012**, *41*, 21 – 31; b) G. Kéranguéven, S. Royer, E. Savinova, *Electrochem. Commun.* **2015**, *50*, 28 – 31.

[28] J. T. Mefford, W. G. Hardin, S. Dai, K. P. Johnston, K. J. Stevenson, *Nat. Mater.* **2014**, *13*, 726 – 732.

[29] K. A. Stoerzinger, M. Risch, B. Han, Y. Shao-Horn, *ACS Catal.* **2015**, *5*, 6021 – 6031.

[30] E. A. Ahmad, V. Tileli, D. Kramer, G. Mallia, K. A. Stoerzinger, Y. Shao-Horn, A. R. Kucernak, N. M. Harrison, *J. Phys. Chem. C* **2015**, *119*, 16804 – 16810.

[31] W. Lee, J. W. Han, Y. Chen, Z. Cai, B. Yildiz, *J. Am. Chem. Soc.* **2013**, *135*, 7909 – 7925.

[32] a) D. Friebel, M. W. Louie, M. Bajdich, K. E. Sanwald, Y. Cai, A. M. Wise, M.-J. Cheng, D. Sokaras, T.-C. Weng, R. Alonso-Mori, R. C. Davis, J. R. Bargar, J. K. Nørskov, A. Nilsson, A. T. Bell, *J. Am. Chem. Soc.* **2015**, *137*, 1305 – 1313; b) K. Sardar, E. Petrucco, C. I. Hiley, J. D. B. Sharman, P. P. Wells, A. E. Russell, R. J. Kashtiban, J. Sloan, R. I. Walton, *Angew. Chem.* **2014**, *126*, 11140 – 11144; c) T. Binninger, R. Mohamed, K. Waltar, E. Fabbri, P. Levecque, R. Kötz, T. J. Schmidt, *Sci. Rep.* **2015**, *5*, 12167.

[33] a) K. A. Stoerzinger, W. Lü, C. Li, Ariando, T. Venkatesan, Y. Shao-Horn, *J. Phys. Chem. Lett.* **2015**, *6*, 1435 – 1440; b) K. A. Stoerzinger, M. Risch, J. Suntivich, W. M. Lu, J. Zhou, M. D. Biegalski, H. M. Christen, Ariando, T. Venkatesan, Y. Shao-Horn, *Energy Environ. Sci.* **2013**, *6*, 1582 – 1588.

[34] a) J. Suntivich, E. Perry, H. Gasteiger, Y. Shao-Horn, *Electrocatalysis* **2013**, *4*, 49 – 55; b) E. Fabbri, R. Mohamed, P. Levecque, O. Conrad, R. Kötz, T. J. Schmidt, *ACS Catal.* **2014**, *4*, 1061 – 1070.

[35] T. J. Schmidt, H. A. Gasteiger, G. D. Stäb, P. M. Urban, D. M. Kolb, R. J. Behm, *J. Electrochem. Soc.* **1998**, *145*, 2354 – 2358.

Manuscript received: October 10, 2015
Accepted Article published: November 27, 2015
Final Article published: December 2, 2015